12th International Symposium on Turbulence and Shear Flow Phenomena (TSFP12)
Osaka, Japan, July 19–22, 2022

PHYSICS BASED TAILORED NUMERICAL GRID FOR STATISTICAL TURBULENCE MODELS BASED ON DISSIPATION ELEMENTS

Fettah Aldudak, Holger Foysi
Department of Mechanical Engineering, University of Siegen
Paul-Bonatz-Straße 9-11, 57076 Siegen, Germany
fettah.aldudak@uni-siegen.de, holger.foysi@uni-siegen.de

ABSTRACT

Since direct numerical simulations (DNS) remain out of reach for most realistic flow conditions, statistical methods as employed in Reynolds Averaged Navier Stokes (RANS), Detached Eddy Simulation (DES) or Large Eddy Simulation (LES) represent an alternative. Regardless of the choice, quality and resolution of the corresponding numerical grid are crucial for the accuracy of a simulation. In the case of DNS, there exists a very well defined requirement in the form of the Kolmogorov length scale η to guide the numerical grid resolution, for example. Unfortunately, for statistical turbulence models, finding the right resolution criterion for automatic grid refinement is more difficult. In addition, real flow conditions require locally adapted, inhomogeneous grids to account for complex flow regimes. In this work, we propose the application of the so-called Dissipation Element (DE) scale ℓ_{DE} and its relation to the Taylor length scale λ as a rough guide for the grid resolution for the use in automatic grid adaptation methods. Both, canonical and realistic complex flows are used to propose a generally applicable condition for the choice of the grid resolution. The present method automatically ensures an adapted resolution throughout the domain with local refinements, minimizing necessary user input to a single quantity.

INTRODUCTION

Generating a high-quality numerical grid is an integral part of the simulation workflow which usually requires a significant amount of time. To ensure grid independent numerical solutions, several cycles of grid generation and subsequent flow simulation are performed iteratively until no substantial changes in the results are observed. Therefore, shortening this effort is accompanied by a reduction of the temporal and computational costs.

The presented method aims at obtaining the targeted grid faster while additionally allowing the appropriate resolution locally. The latter is essential for the efficiency since refinement is performed only where necessary. In a similar manner to DNS resolution down to the Kolmogorov length η, we intend to find a physically-based length scale for turbulence models to adapt the grid resolution based on physics. Ideally, a universally valid magnitude of this length scale should directly emanate from the flow physics without the need of further user input. Thus, adapting the resolution to this global value will lead to the desired unique mesh for the flow under consideration which is ready to use for the final simulation.

We propose the Dissipation Element (DE) to be such a unique, physically-based length scale. These intermediate spatial structures associated with turbulent scalar fields can be identified by connecting corresponding pairs of zero-gradient extremal points. Finite-length gradient trajectories starting from every point in the scalar field in the directions of ascending and descending scalar gradients will always reach a minimum and a maximum point. A DE is defined by all points along the trajectories belonging to the same pair of extremal points. Hence, DEs directly originate from the turbulent flow and, at the same time, are irregularly shaped and space-filling. This means that a turbulent scalar field can be completely decomposed into such elements with no empty space in between. Velocity components, turbulent kinetic energy k and its dissipation rate ε can be chosen for such a decomposition. The DE concept has been introduced first by Peters & Wang (2006) who analysed small-scale statistics from passive scalar fields of homogeneous shear turbulence obtained from DNS. For this flow case, Wang & Peters (2006) report that the mean DE length ℓ_{DE} is of the order of the Taylor scale defined as $\lambda = (10\nu k/\varepsilon)^{1/2}$ where ν is the kinematic viscosity, k the turbulent kinetic energy and ε the dissipation rate. As the DE length scales cannot be derived accurately when using RANS, for example, a relationship like this would allow us to base the length scale determination on a quantity easily accessible even in statistical simulations.

The DE methodology has been further applied within DNS of canonical turbulent channel flow by companion works of Aldudak & Oberlack (2009), Aldudak & Oberlack (2011), Aldudak & Oberlack (2012) and Aldudak (2012). The strong influence of rigid walls on the flow geometry and structures has been examined showing a distinct dependency of the DE length on the wall-normal direction. It was shown that ℓ_{DE} increases linearly in the wall-normal direction y, starting from the logarithmic region, until a constant length is reached in the channel center, due to decreasing shear. Interestingly, this linear behaviour occurs mainly in the intermediate region between the inner and outer layers, where the turbulent production of k and its dissipation ε are approximately equal at sufficiently high Reynolds numbers (Hinze, 1975). This region is roughly located between $y^+ = u_\tau y/\nu = 30$ and $y/h = 0.7$ (Aldudak, 2012). This is in good agreement with the findings in Lee & Moser (2015) where the balance of production and dissipation of k in a turbulent channel flow DNS at $Re_\tau = u_\tau h/\nu = 5200$ is plotted against the wall-normal direction. Here, h is the channel half width, $u_\tau = \sqrt{\tau/\rho}$ is the friction velocity and τ and ρ are the mean wall friction and density, respectively. The region of relative balance coincides well with the above-mentioned range of linear increase of the mean DE length scale. Furthermore, it is found that the DE length scale decreases with increasing Reynolds number Re, i.e. $\ell_{DE} = f(y, Re)$, similar to the Taylor length λ. Given the space-filling nature of the DEs, this means that the number of generated structures in a wall-bounded turbulent flow decreases with wall distance and increases with Reynolds number.

In Aldudak (2012), we investigated the relation between DE and classical length scales, especially the intermediate

Taylor length. It was found that the DE length is proportional to the Taylor scale in turbulent channel flows almost over the entire channel height ($\ell_{DE} \sim \lambda$). To find an expected value for the proportionality factor, we plot the ratio ℓ_{DE}/λ as a function of wall-normal distance for the friction based Reynolds number $Re_\tau = 720$. The three plots represent the ratio between DE and Taylor scales for individual velocity components, respectively. As seen in figure 1, ℓ_{DE}/λ doesn't vary widely after the start of the logarithmic region at about $y/h \approx 0.04$, with the proportionality factor being between 2 and 3 for a large wall-normal extent. An increase can be observed close to the wall towards the start of the logarithmic and subsequently buffer layer, where the production peaks, too. Although each length scale itself exhibits a clear y dependency, their quotient appears to be widely independent of the wall-normal direction throughout a large part of the channel height. This observation is a direct indication that the dissipation element length scale can be determined to good approximation by making use of the Taylor microscale, which is readily available even in Reynolds averaged simulations, for example. Since the grids were often including points within the buffer layer, too, the criterion for grid refinement was chosen to require cells sizes following the inequality

$$\Delta < \ell_{DE} \approx 3 \cdot \lambda, \tag{1}$$

to reflect the increase of ℓ_{DE}/λ close to the wall. This inequality is not exact but turned out to give nice results in various numerical experiments.

To verify the ability of the proposed method several canonical and more realistic test cases were simulated using RANS and DES. So far, the test cases included plane turbulent channel flow (not shown here), a surface-mounted cube in a channel (Martinuzzi & Tropea (1993)), an Ahmed body generic car configuration (Ahmed et al. (1984)) and a more demanding case of a passenger car (DrivAer, Heft et al. (2012a)). The latter cases exhibit complex flow structures with large separation and recirculation regions as well as sudden changes in gradients. At the same time, they are also well-known benchmarks, thus suitable for validation purposes.

RESULTS

A solver in the framework of OpenFOAM (Weller et al. (1998)) was extended to identify and automatically refine numerical cells during the simulation process, whose size violated inequality (1).

(i) Initially, a very coarse mesh with uniform grid cell size was created to serve as a starting numerical grid. The cells are cubic so that the length of the cell, Δ, is calculated using the cubic root of the individual cell volume.

(ii) After the simulation reached an intermediate steady state, the algorithm is refining all those cells further, which exceed the resolution criterion. Cells smaller than half the resolution-criterion are coarsened.

(iii) After every refinement step, the old solution is interpolated linearly onto the new mesh by the solver and the computation is resumed until a new intermediate steady state is reached.
Step (ii) and (iii) are repeated, until all cells fulfill the resolution criterion and steady state is reached.

The algorithm was capable of successfully producing ready-for-use grids with well-distributed local refinement regions using inherent flow physics only.

A surface mounted cube (Martinuzzi & Tropea (1993)) was simulated using RANS, where no-slip boundary condition was applied to the horizontal top, bottom walls and the cube, respectively. The Reynolds number based on the cube height H was chosen to be $Re_H = 40000$. The spatial dimensions in the streamwise, spanwise and wall-normal directions were $19.5H \times 9H \times 2H$. Further information can be found in Martinuzzi & Tropea (1993) where the flow was investigated experimentally. Figure 2(i) depicts the coarse initial grid using uniform cubic cells starting the simulation. Figure 2(ii) instead shows the final grid where all cells were refined to fulfill the resolution criterion in (1). Near the walls and around the cube, as well as in regions with large gradient, the refinement level is highest, transitioning to less refined regions using consecutive refinement levels, as expected. Figure 2(iii) shows results of the velocity obtained from the unsteady *k-ω-SST* RANS (Langtry & Menter, 2009) and Spalart-Allmaras-IDDES DES (Gritskevich et al., 2012) simulations performed with OpenFOAM and our grid refinement procedure, demonstrating good agreement with experimental data from Martinuzzi & Tropea (1993).
In a similar manner, flow past an Ahmed body (Ahmed et al. (1984)) configuration with a 25° slanted back face was calculated with *k-ω-SST* RANS which, in spite of its simple geometry, exhibits complex flow aspects associated with car aerodynamics such as a counter-rotating vortex pair and a strong separation and recirculation region. The Reynolds number based on the length of the body was $Re = 2.8 \times 10^6$. Figure 3(i) shows two recirculation bubbles, as expected, together with the case-specific tailored mesh and the corresponding velocity profiles compared with experimental data. The tailored grid shows refinement regions of different intensity according to the resolution criterion in Equation 1 with finer cells near walls as well as separation zones. The typical longitudinal counter-rotating vortices (Lienhart et al. (2002)) in the body wake are accounted for by the grid refinement process. In the last figure, mean velocity profiles obtained from RANS simulations are plotted together with measurements from Lienhart et al. (2002) at selected positions along the symmetry plane on the slant and in the wake of the Ahmed body. The profiles are in good agreements with the experiments, especially in the wake regions with recirculation, whereas near the trailing edge of the slant small deviations are visible.

Since the two aforementioned geometries are rather simple, the more demanding case of a passenger car has been used to further validate the proposed tailored mesh approach. With this test case we intend to demonstrate the efficiency of this new method further for relevant, complex flow problems. As a configuration the realistic DrivAer car model is chosen which was introduced by Heft et al. (2012b). Its modular geometry with three different rear end configurations, i.e. estate back, notchback, and fastback, allows for aerodynamic research on realistic passenger cars. Details of varying degree, such as mirrors, wheel rims and a detailed underbody can be added. Different combinations of DrivAer models have been investigated both numerically and experimentally making it eligible for validation studies. For the present work, the fastback variant with smooth underbody, side mirrors and detailed wheels is utilized and results are compared with available data. As before, an initial numerical grid is generated first which is adapted to the shape of the car and consists of hexaeder-dominant coarse cells. A precursor simulation has been conducted to provide appropriate turbulent inflow profiles. Subsequently, a first simulation has been performed, yielding the cell to Taylor length ratio, Δ/λ, as the key parameter for local refinement. Based on

this quantity, all cells exceeding the criterion in Equation 1 are identified and refined accordingly. Thereby, the desired final mesh with appropriate resolution is obtained and can be used for further simulations. The Reynolds number based on the car length is set to 4.87×10^6 which was investigated experimentally by Heft et al. (2012b), Strangfeld et al. (2013)) and numerically by Rüttgers et al. (2019), Ekman et al. (2020), for example. The final mesh for a symmetric half-body contains 53 Million cells with the first wall boundary layer located in the lower logarithmic layer, hence, giving rise to the use of standard wall functions. The size of the mesh is comparable to that used in a Large-Eddy-Simulation with 55 Million cells, discussed in Rüttgers et al. (2019). The mean inflow velocity is 16 m/s and a no-slip boundary condition is applied on rigid walls. The two-equation $k-\omega-$SST turbulence model has been employed for a steady-state RANS simulation.

Figure 4 shows iso-contours of two regions with the highest refinement levels which are identified by the tailored mesh approach. The purple region around the side mirrors and the near-wake marks the finest grid resolution and is located in the recirculation region which normally forms behind bluff bodies. Mirrors, wheels and the rear end are zones where elongated vortical structures are expected, see Rüttgers et al. (2019). The larger gray iso-surface starts from the wheels and the side mirrors and encloses large areas around the car. Note, that typical counter-rotating longitudinal vortex regions in the wake are detected for proper resolution, illustrating the physically-based nature of the proposed method. As before, individual refinement regions are created with smooth transitions as seen in Figure 5 and the zoomed region behind the car in the same figure.

In image 6, streamlines based on the averaged velocity on the symmetry plane are depicted together with the wake isoline (black) where the streamwise velocity is zero, highlighting the common recirculation zone in the near-wake (Rüttgers et al. (2019), Ekman et al. (2020), Strangfeld et al. (2013)). Moreover, streamlines coming from the upper part form a small separation zone towards the end of the rear window. Additionally, the pressure coefficient defined as

$$C_p = \frac{p - p_\infty}{0.5 \rho U_\infty^2}$$

is plotted on the car surface where U_∞, p_∞, and ρ are inflow velocity, freestream pressure and and air density, respectively. In order to look at the pressure distribution in more detail and compare to the literature, C_p is shown in figure 7 for various streamwise positions along the car determined at the symmetry plane. Experimental data from Heft et al. (2012b) and numerical results of a LES by Rüttgers et al. (2019) are compared here to the present RANS results obtained with the tailored grid method. Figure 7(a) shows the distribution of the pressure coefficient C_p along the symmetry line of the DrivAer car at the top surface. A good overall agreement of our RANS results with both experiments and LES data can be seen. At the stagnation point at the vehicle front a high pressure is observed, decreasing rapidly first due to the acceleration of the flow. Along the adjacent engine bonnet, the pressure increase is replicated appropriately. Additionally, the distribution around the cowl top, showing a small kink in the C_p distribution around $x/L = 0.3$, is reproduced nicely with good accuracy, where separation and reattachment occur. Arriving at the car roof, both LES and RANS deviate by the sudden pressure change and underpredict the pressure. To some extent, this deviation can be caused by the support holding the car in the experimental installation (Heft et al. (2012a), Ashton et al. (2016)). The pressure distribution is close to the experimental data until the trailing edge of the rear end. While the LES results match the measurements more accurately, minor deviations in RANS are visible. Similarly, figure 7(b) illustrates the pressure distribution at the bottom of the symmetry plane. A pronounced difference between the measurements and simulation data in general is observed initially, where the measured C_p decreases sharply. Similarly to the top of the car, the RANS results exhibit an overall good agreement with LES and experimental data, validating the automatic grid refinement procedure.

CONCLUSIONS

A novel tailored grid approach has been introduced, where Dissipation Element (DE) length scales ℓ_{DE}, obtained by DNS results, serve as grid resolution criterion. Previous work has been discussed to underline the relation between DE and the well-known Taylor length scale (λ) which is usually available to statistical simulation methods. Based on results from turbulent channel flow simulations, where both length scales can be accurately determined, it was found that the relation of DE and Taylor length scale ℓ_{DE}/λ is varying only to a minor degree over most of the channel width, starting with the logarithmic region. This allows determining ℓ_{DE} via the Taylor scale to automatically refine the grid whenever the grid cells surpass a predetermined threshold based on ℓ_{DE}.
Benchmarks and test cases such as a wall-mounted cube, Ahmed body and a more realistic DrivAer passenger car have been analyzed by applying the proposed meshing method. In all cases it could be observed that, by applying the resolution criterion, a well-formed numerical grid with smooth transition emerged with no further involvement required externally. The resulting numerical grids are shown to follow physical characteristics of the underlying turbulent flow closely and are capable of reproducing the validation results with appropriate accuracy. Contrary to classical meshing techniques, expensive grid independence studies can be reduced to a minimum. Since scale-resolving simulations tend to DNS with increasing resolution, this proposed resolution criterion could serve as a good compromise between direct resolution and modelling. Nevertheless, further analysis is needed to investigate the tailored grid approach in conjunction with LES and DES.

REFERENCES

Ahmed, S.R., Ramm, G. & Faltin, G. 1984 Some salient features of the time-averaged ground vehicle wake. In SAE International Congress and Exposition. SAE International.

Aldudak, F. 2012 Geometrical structure of small scales and wall-bounded turbulence. PhD thesis, TU Darmstadt, Darmstadt, Germany.

Aldudak, F. & Oberlack, M. 2009 Dissipation element analysis of scalar fields in wall-bounded turbulent flow. Proceedings of EUROMECH Colloquium 512, pp. 9–11.

Aldudak, Fettah & Oberlack, Martin 2011 Length scale analysis in wall-bounded turbulent flow by means of dissipation elements. J. of Physics: Conf. Series **318** (2), 022001.

Aldudak, F. & Oberlack, M. 2012 Dissipation element analysis in turbulent channel flow. J. Fluid Mech. **694**, 332–351.

Ashton, N., West, A., Lardeau, S. & Revell, A. 2016 Assessment of rans and des methods for realistic automotive models. Computers Fluids **128**, 1–15.

Ekman, P., Wieser, D., Virdung, T. & Karlsson, M. 2020 Assessment of hybrid rans-les methods for accurate automotive aerodynamic simulations. Journal of Wind Engineering and Industrial Aerodynamics **206**, 104301.

Gritskevich, M.S., Garbaruk, A.V. & Schütze, J. 2012 Development of ddes and iddes formulations for the $k-\omega$ shear stress transport model. Flow Turbulence Combust. **88**, 431–449.

Heft, Angelina I., Indinger, Thomas & Adams, Nikolaus A. 2012a Experimental and numerical investigation of the drivaer model. Fluids Engineering Division Summer Meeting, vol. Volume 1: Symposia, Parts A and B, pp. 41–51.

Heft, Angelina I., Indinger, Thomas & Adams, Nikolaus A. 2012b Introduction of a new realistic generic car model for aerodynamic investigations. In SAE 2012 World Congress Exhibition. SAE International.

Hinze, J. O. 1975 Turbulence. McGraw-Hill Book Company.

Langtry, Robin B. & Menter, Florian R. 2009 Correlation-based transition modeling for unstructured parallelized computational fluid dynamics codes. AIAA Journal **47** (12), 2894–2906.

Lee, Myoungkyu & Moser, Robert D. 2015 Direct numerical simulation of turbulent channel flow up to re_τ=5200. Journal of Fluid Mechanics **774**, 395–415.

Lienhart, Hermann, Stoots, C & Becker, S. 2002 Flow and turbulence structures in the wake of a simplified car model (ahmed model). Notes on Numerical Fluid Mechanics **77**.

Martinuzzi, R. & Tropea, C. 1993 The Flow Around Surface-Mounted, Prismatic Obstacles Placed in a Fully Developed Channel Flow. J. of Fluids Engineering **115** (1), 85–92.

Peters, N. & Wang, L. 2006 Dissipation element analysis of scalar fields in turbulence. C. R. Mech. **334**, 493–506.

Rüttgers, Mario, Park, Junshin & You, Donghyun 2019 Large-eddy simulation of turbulent flow over the drivaer fastback vehicle model. Journal of Wind Engineering and Industrial Aerodynamics **186**, 123–138.

Strangfeld, Christoph, Wieser, Dirk, Schmidt, Hanns-Joachim, Woszidlo, Rene, Nayeri, Christian & Paschereit, Christian 2013 Experimental study of baseline flow characteristics for the realistic car model drivaer. In SAE 2013 World Congress Exhibition. SAE International.

Wang, L. & Peters, N. 2006 The length scale distribution function of the distance between extremal points in passive scalar turbulence. J. Fluid Mech. **554**, 457–475.

Weller, H. G., Tabor, G., Jasak, H. & Fureby, C. 1998 A tensorial approach to computational continuum mechanics using object-oriented techniques.

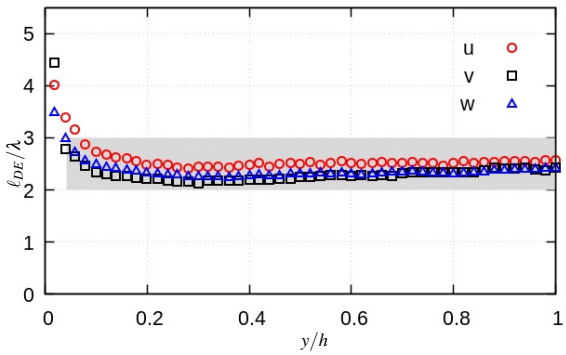

Figure 1: Proportionality relation between DE and classical Taylor length scales for $Re_\tau = 720$ over wall-normal distance y/h obtained from DNS results (Aldudak, 2012). Gray area starts at the log-layer and marks the broad region of validity for the refinement condition.

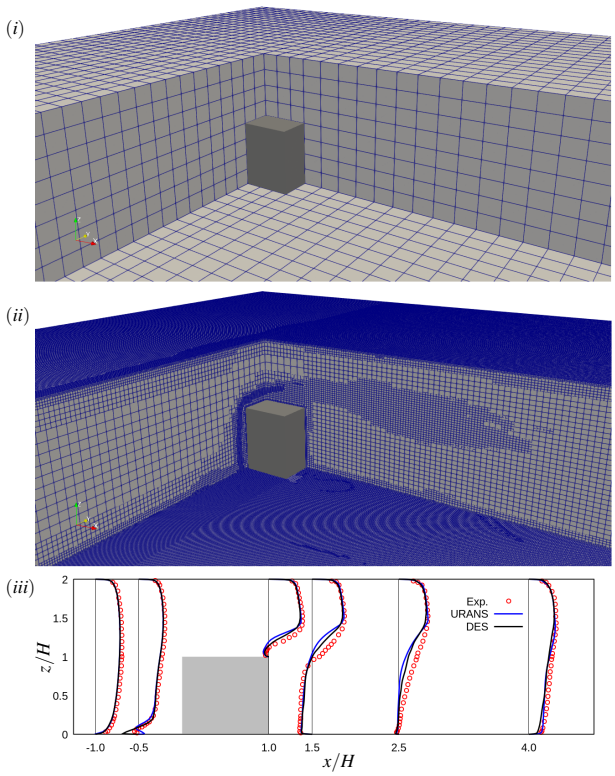

Figure 2: Wall mounted cube: (i) Starting grid. (ii) Tailored grid after refinement. (iii) Velocity profiles at selected positions, comparison to experimental data of Martinuzzi & Tropea (1993).

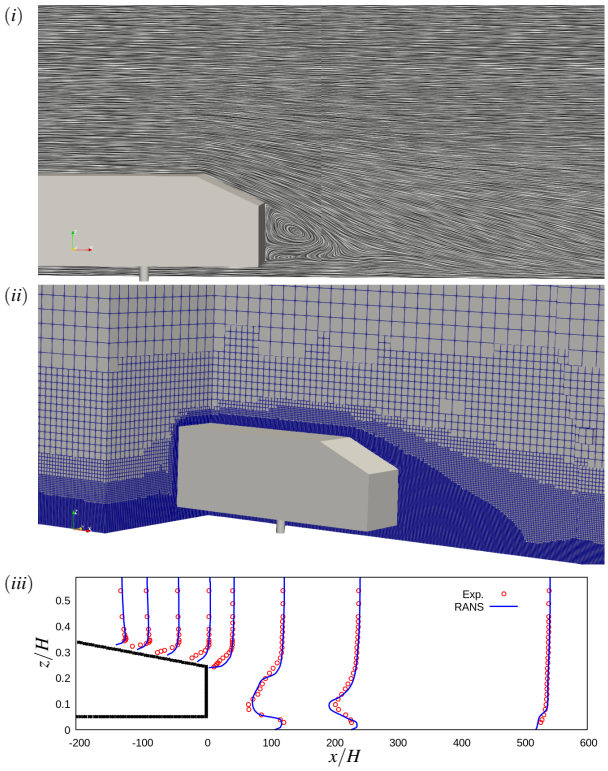

Figure 3: (i) Streamlines at the center plane. (ii) Tailored grid after automatic refinement. (iii) Velocity profiles at selected positions in comparison to data from Lienhart et al. (2002).

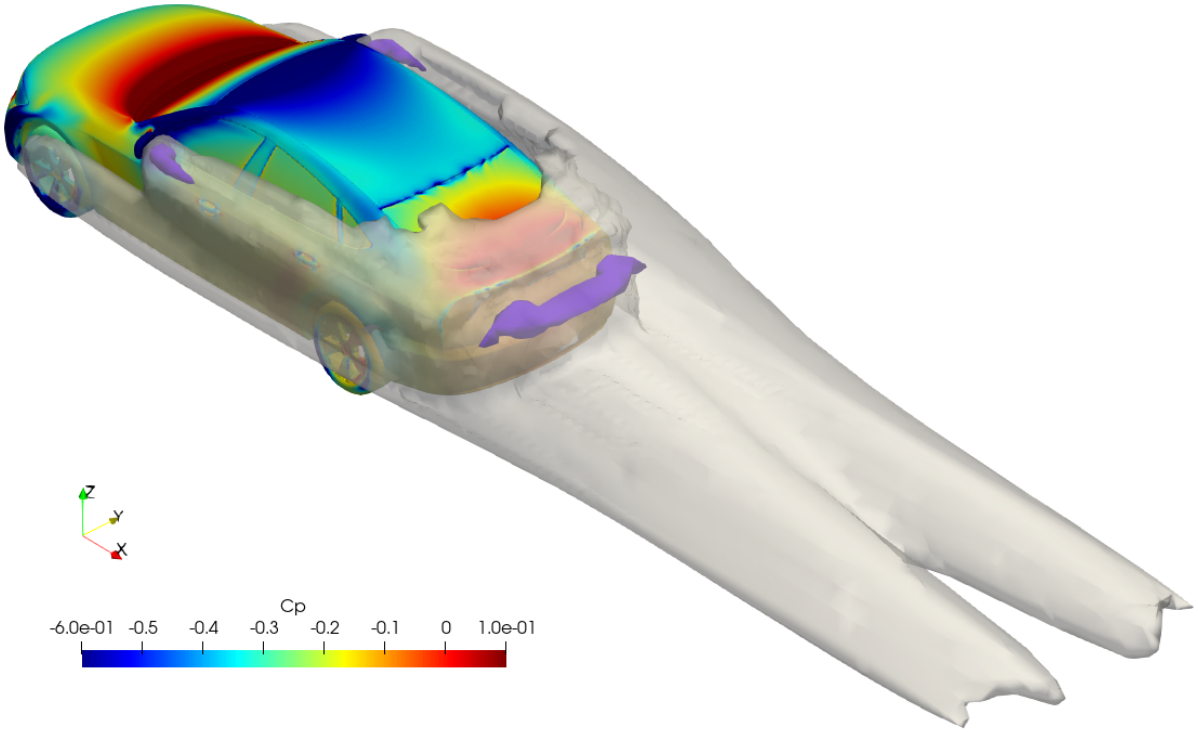

Figure 4: Illustration of the highest refinement regions. The light grey colors represent the second finest grid region, the purple region the finest grid cells. Those are located behind the side mirrors and tail of the car. Contours of C_p are depicted on the car surface.

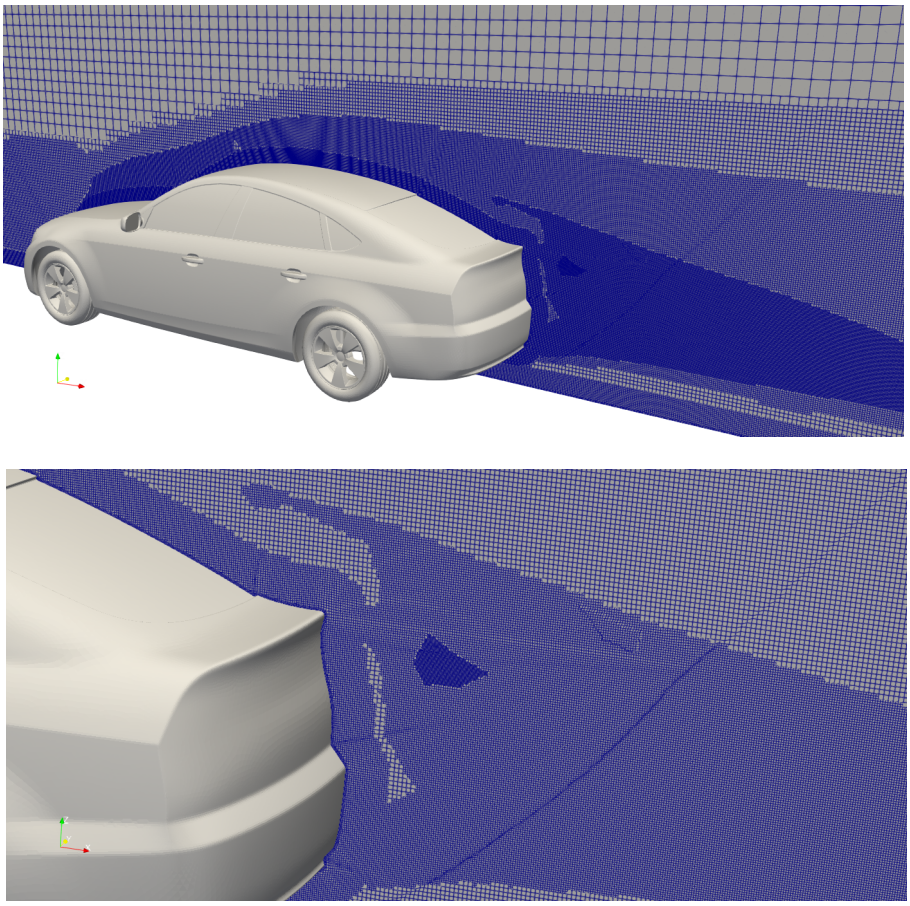

Figure 5: Tailored grid of the fastback DrivAer configuration (Heft et al. (2012a)) in the symmetry plane, showing different levels of refinement. Top: Tailored grid, complete car. Bottom: Zoom into the tail section of the car.

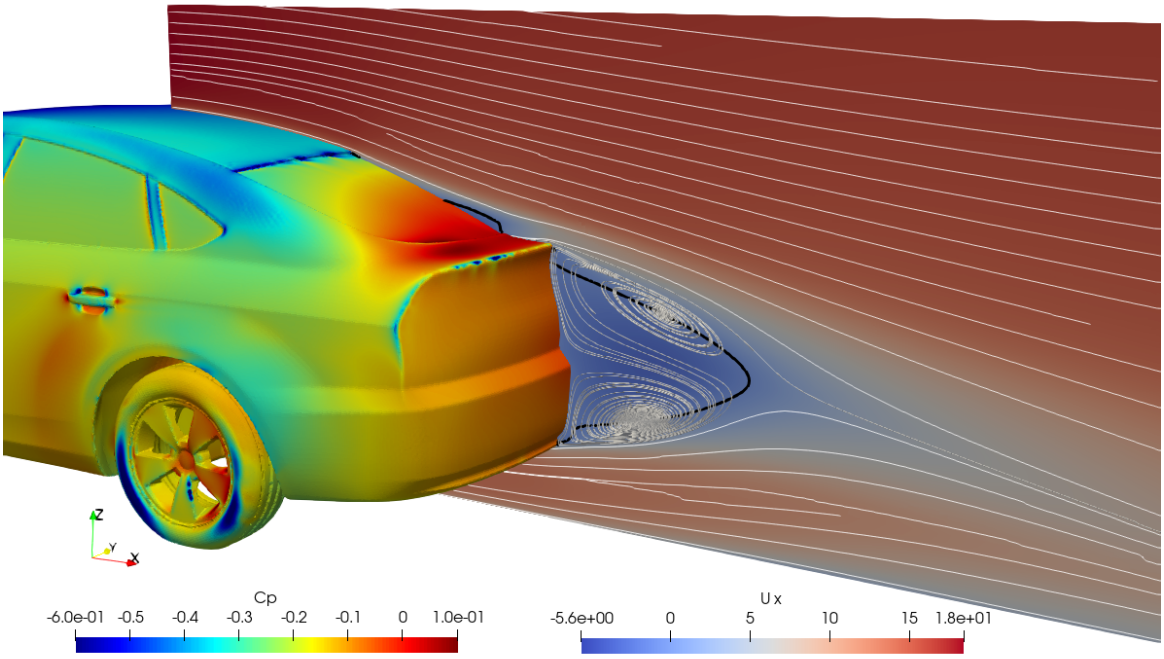

Figure 6: Surface pressure coefficient distribution, mean velocity streamlines along the symmetry plane and wake isoline $U_x = 0$ (black).

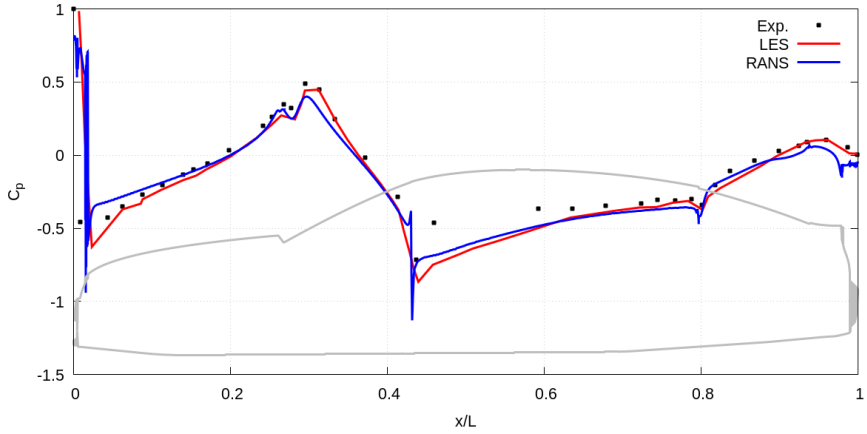

(a) Pressure coefficient at the top surface.

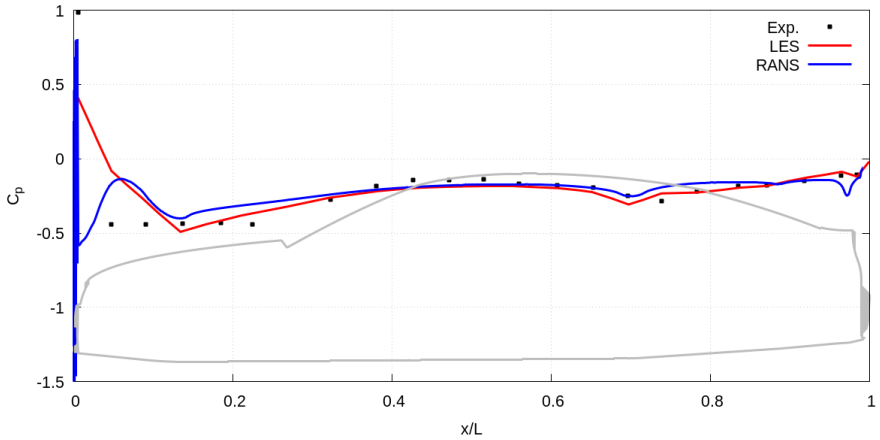

(b) Pressure coefficient at the bottom surface.

Figure 7: Pressure coefficient distributions along the symmetry plane of the DrivAer car (indicated in grey), for the top (a) and bottom (b) surface, compared to experiments (Heft et al. (2012a)) and LES simulations (Rüttgers et al. (2019)). L indicates the length of the car.